Archives of Biochemistry and Biophysics 570 (2015) 47–57

Contents lists available at ScienceDirect

Archives of Biochemistry and Biophysics

journal homepage: www.elsevier.com/locate/yabbi

Catalytic activity of human indoleamine 2,3-dioxygenase (*h*IDO1) at low oxygen

Ayodele O. Kolawole [1], Brian P. Hixon [2], Laura S. Dameron, Ian M. Chrisman, Valeriy V. Smirnov *

Department of Chemistry and Biochemistry, Center for Biomolecular Structure and Dynamics, University of Montana, Missoula, MT 59812, United States

ARTICLE INFO

Article history:
Received 25 November 2014
and in revised form 12 February 2015
Available online 21 February 2015

Keywords:
Indoleamine dioxygenase
Oxygen electrode
Enzyme kinetics
Substrate analog
Inhibition
Global fit

ABSTRACT

A cytokine-inducible extrahepatic human indoleamine 2,3-dioxygenase (*h*IDO1) catalyzes the first step of the kynurenine pathway. Immunosuppressive activity of *h*IDO1 in tumor cells weakens host T-cell immunity, contributing to the progression of cancer. Here we report on enzyme kinetics and catalytic mechanism of *h*IDO1, studied at varied levels of dioxygen (O_2) and L-tryptophan (L-Trp). Using a cytochrome b_5-based activating system, we measured the initial rates of O_2 decay with a Clark-type oxygen electrode at physiologically-relevant levels of both substrates. Kinetics was also studied in the presence of two substrate analogs: 1-methyl-L-tryptophan and norharmane. Quantitative analysis supports a steady-state rather than a rapid equilibrium kinetic mechanism, where the rates of individual pathways, leading to a ternary complex, are significantly different, and the overall rate of catalysis depends on contributions of both routes. One path, where O_2 binds to ferrous *h*IDO1 first, is faster than the second route, which starts with the binding of L-Trp. However, L-Trp complexation with free ferrous *h*IDO1 is more rapid than that of O_2. As the level of L-Trp increases, the slower route becomes a significant contributor to the overall rate, resulting in observed substrate inhibition.

Introduction

In the human body, L-tryptophan (L-Trp) is one of the nine essential dietary amino acids [1]. It functions as a building block of proteins and as a precursor of niacin, an intermediate in the biosynthesis of NAD^+ [2], and serotonin, a mood-modulating neurotransmitter and physiological regulator [3]. Up to 90% of dietary L-Trp is catabolized via the kynurenine pathway [4,5]. The kynurenine pathway starts with a dioxygenation reaction of L-Trp that is catalyzed by indoleamine 2,3-dioxygenase (IDO) and tryptophan 2,3-dioxygenase (TDO) [6,7]. Both IDO and TDO contain a type-*b* heme and use dioxygen (O_2) to open the five-membered ring of L-Trp to form N-formyl-L-kynurenine (NFK), as shown in Scheme 1 [6]. Excessive exhaustion of L-Trp via the kynurenine pathway significantly hinders T-cell proliferation, differentiation, effector function, and viability, resulting in a suppressed immune response [8]. Catabolites of L-Trp are capable of promoting immunosuppression and tumor tolerance during cancer [9], formation of cataracts [10,11], HIV-related neurological damage, and ischemic brain injury [12].

IDO is induced extrahepatically throughout the body [6]. The strongest inducer of IDO is a proinflammatory cytokine interferon-γ (IFN-γ) [13]. IDO-initiated L-Trp degradation accelerates during conditions that cause cellular activation of the immune response such as malignancy, inflammation, autoimmune disorder, and pregnancy [12]. The induction of IDO by IFN-γ is greatly diminished in a hypoxic environment, where the O_2 concentration is between 5% and 10% of air-saturation level [14–16]. During hypoxia, cells stimulated with IFN-γ demonstrate reduced levels of IDO compared to normoxic conditions. IDO antimicrobial and immunoregulatory functions are also significantly impaired [14–16].

Even under normoxic conditions, the physiological levels of O_2 are quite low (between 14% and 24% of air-saturation level or between ~35 μM and ~65 μM O_2) [17]. The steady-state kinetic data for IDO are known primarily in solutions saturated with air [18–28]. Here, we report on enzyme kinetic studies of human IDO isoform-1 (*h*IDO1)[3] (EC 1.13.11.52) at physiologically-relevant levels of O_2 as a function of both substrates – O_2 and L-Trp. This

* Corresponding author.
E-mail address: valeriy.smirnov@umontana.edu (V.V. Smirnov).
[1] Present address: Department of Biochemistry, Federal University of Technology, P.M.B. 704, Akure 340001, Nigeria.
[2] Present address: National Foundation for Fertility Research.

[3] *Abbreviations used:* *h*IDO1, human indoleamine 2,3-dioxygenase isoform-1; TDO, tryptophan 2,3-dioxygenase; L-Trp, L-tryptophan; 1-Me-L-Trp, 1-methyl-L-tryptophan; NFK, N-formyl-L-kynurenine; O_2, dioxygen; $O_2^{\cdot-}$, superoxide anion; H_2O_2, hydrogen peroxide; NHM, norharmane (β-carboline); IFN-γ, interferon-γ; NAD^+, nicotinamide adenine dinucleotide; β-NADH, β-nicotinamide adenine dinucleotide hydride; Cu,Zn-SOD, copper-zinc superoxide dismutase; DNase I, deoxyribonuclease I; IPTG, isopropyl β-D-1-thiogalactopyranoside; PMSF, phenylmethylsulfonyl fluoride; EDTA, ethylenediaminetetraacetic acid; MOPS, 3-(N-morpholino)propanesulfonic acid; SDS–PAGE, sodium dodecyl sulfate polyacrylamide gel electrophoresis; LRF MALDI-TOF, linear-reflectron matrix-assisted laser desorption/ionization time-of-flight mass spectrometer.

http://dx.doi.org/10.1016/j.abb.2015.02.014
0003-9861/

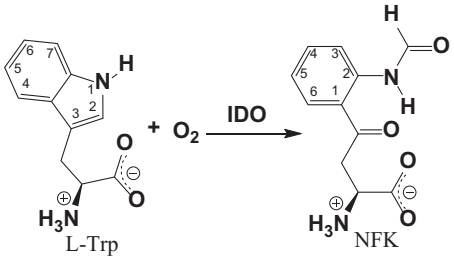

Scheme 1. Reaction catalyzed by IDO.

information is vital for understanding enzyme-substrate interactions in *h*IDO1 and for designing inhibitors with enhanced therapeutic responses [29–31]. Using a new assay methodology, we quantify the effects of O_2 concentration on the initial rates of *h*IDO1 catalysis. We analyze the data within a mechanistic model that allows for initial complexation of either O_2 or L-Trp with a free ferrous form of *h*IDO1 – $^{Fe(II)}$*h*IDO1 [6,23]. This model also considers that both resulting substrate-bound species – $^{Fe(III)}$*h*IDO1·O_2^- and $^{Fe(II)}$*h*IDO1·L-Trp [32], lead to a ternary complex – *h*IDO1·O_2·L-Trp.

The ternary complex has been previously characterized in human and rabbit IDO by the stepwise mixing of substrates with the ferrous enzyme either manually, at a low temperature, or on a stopped-flow, at room temperature [24–28,33,34]. Here we analyze the kinetics of the formation of the ternary complex. We observe that under steady-state conditions, the ternary complex forms via two separate pathways. Even though the O_2-first/L-Trp-second addition route is faster than the L-Trp-first/O_2-second path [23,35], the organic substrate binds to the free ferrous *h*IDO1 at a higher rate than O_2 [35]. At low physiologically-relevant concentrations of both substrates, the slower L-Trp-initiated pathway is a significant contributor to the overall catalytic rate, resulting in pronounced substrate inhibition of catalysis. Such kinetic control of *h*IDO1 activity could be operational *in vivo* where, depending on tissue oxygenation [17], O_2 supply may be limited relative to L-Trp level [36,37].

Materials and methods

Reagents

L-tryptophan (Cat. # T0254), β-NADH (Cat. # N1161), Cu,Zn-SOD (Cat. # S8160), catalase (Cat. # C100), lysozyme (Cat. # L6876), DNase I (Cat. # D5025), PMSF (Cat. # P7626), Trizma (Cat. # T1503), MOPS (Cat. # M3183), imidazole (Cat. # 56750), EDTA (Cat. # ED4SS), kanamycin sulfate (Cat. # K1377), 1-methyl-L-tryptophan (Cat. # 447439), norharmane (Cat. # N6252) and norharmane hydrochloride (Cat. # N6377) were from Sigma–Aldrich; agar (Cat. # N833) and yeast extract (Cat. # J850) were from Amresco; tryptone (Cat. # 95039) was from Fluka; sodium chloride (Cat. # SX0425), monobasic sodium phosphate (Cat. # SX0710), dibasic sodium phosphate (Cat. # SX0715) were from EMD; δ-aminolevulinic acid hydrochloride (Cat. # 01433) and IPTG (Cat. # 00194) were from Chem-Impex International, Inc. in Wood Dale, IL; N_2 (pre-purified grade) and O_2 (USP grade) were from Norco, Inc. in Boise, ID. The pETevIDO plasmid for *h*IDO1 expression and the plasmids for cytochrome b_5 and cytochrome b_5 reductase were kindly provided by Prof. A. Grant Mauk (University of British Columbia).

Enzyme preparation

*h*IDO1 (EC 1.13.11.52) was overexpressed in One Shot BL21 Star (DE3) chemically competent *Escherichia coli* cells (Invitrogen) using a published procedure [38]. Greater than 95% homogeneity of *h*IDO1 was confirmed by the SDS–PAGE after the second Ni-affinity column and dialysis into 50 mM Tris·HCl pH 8.0 buffer, containing 100 mM NaCl and 4 mM EDTA. The purified enzyme exhibited an $[M+H]^+$ peak at m/z = 45,586 on a Microflex LRF MALDI-TOF mass spectrometer (Bruker), which is in good agreement with the expected value of m/z = 45,643. Cytochrome b_5 and cytochrome b_5 reductase, overexpressed in One Shot BL21 Star (DE3) cells, were purified as described elsewhere [39,40]. The homogeneity of these proteins was confirmed by 10% SDS–PAGE analysis. Protein concentrations were determined spectrophotometrically. All enzyme stocks were stored at −75 °C.

Measurement of initial rates of hIDO1 catalysis by monitoring O_2 consumption

Initial rates of *h*IDO1 catalysis of L-Trp dioxygenation were measured at 25.0 °C using a Clark-type oxygen electrode consisting of a digital ammeter (Biological Oxygen Monitor, model 5300A, Yellow Springs Instruments (YSI)) and a polarographic oxygen probe (5331A, YSI). Highly reproducible O_2 depletion traces (Fig. S1) [41] were recorded in a reaction chamber thermostated on a modified bath assembly (5301B, YSI) interfaced to a recirculating water bath (DC10, Thermo Scientific; K20, Haake). A VWR 10″ × 10″ professional stirrer was used to maintain the stirring rate at 700 rpm. O_2 and N_2 gases were metered using a Riteflow flow meter (PMR1-010976, Bel-Art Scienceware). This experimental setup allowed for precise control of temperature, stirring rate, and oxygen level. The oxygen probe was calibrated daily to the dissolved oxygen in air-saturated water (resistivity ⩾18.2 MΩ × cm) at normal pressure. Due to the elevation of Missoula, the 100% air-saturation level of pure water at 25.0 °C corresponds to $[O_2]$ = 230 μM, which is lower than $[O_2]$ = 258 μM at sea level [42]. Solubility of O_2 was calculated using atmospheric pressure measured with a mercury manometer interfaced to a high-vacuum line (Chemglass). Atmospheric pressure at sea level was taken as 760 mmHg [42].

A typical reaction mixture (3.000 mL) contained 20 mM MOPS buffer at pH 7.0, 150 μM β-NADH, 1.0 μM cytochrome b_5, 140 nM cytochrome b_5 reductase, 54 nM Cu,Zn-SOD, 12 nM catalase, and varying concentrations of L-Trp [43]. The solution was equilibrated against air or a mixture of pure O_2 and N_2, saturated with water vapor at atmospheric pressure by passing through a fritted gas washing bottle (Chemglass, Cat. # CG-1114-13). During inhibition studies, the reaction mixture was also supplemented with 3–15 μL of inhibitor stock solution to the final inhibitor concentration of 1–5 μM. Inhibitor stocks (100 mL of 1.00 mM solution of either 1-methyl-L-tryptophan or norharmane hydrochloride) were prepared in 100 mM potassium phosphate buffer at pH 7.0. The reaction was initiated by injecting a 5-μL aliquot of *h*IDO1 stock (~120 μM) into a reaction chamber to an expected final concentration of ~200 nM, using a gas-tight syringe (Hamilton). The exact concentrations of *h*IDO1 stock solutions were measured spectrophotometrically on an AVIV Model 14 Spectrophotometer (Aviv Biomedical), or a NanoDrop 2000 (Thermo Scientific) using molar absorptivity $\varepsilon_{\lambda=404nm}$ = 172,000 M^{-1} cm^{-1} [44]. Initial rates of O_2 consumption were measured in the range of the steepest $[O_2]$ decline (12 s long), normally 2–4 s after injecting the ferric *h*IDO1. All measurements were performed in triplicate or greater. Readouts of the oxygen probe were transmitted to a PC workstation with a 1-Hz sampling rate. The slopes of the oxygen consumption traces were determined in Excel 2010 (Microsoft) and their absolute values were expressed in μM/s. These initial velocities of O_2 consumption were converted to specific activity of *h*IDO1 by dividing by the exact final micromolar enzyme concentration – $[hIDO1]_T$. All nonlinear

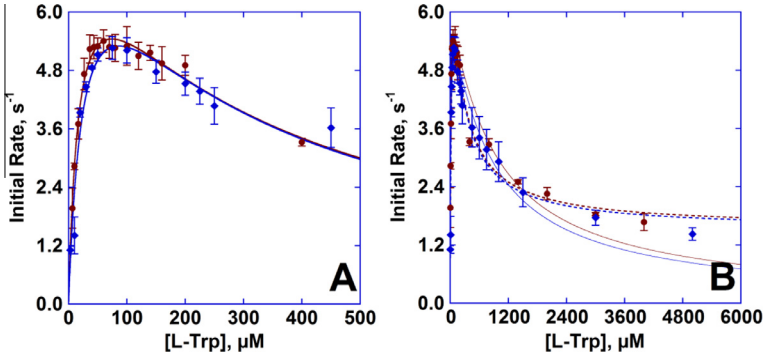

Fig. 1. Initial rates of *h*IDO1 catalysis as a function of L-Trp concentration at 25.0 °C. Conditions: 20 mM air-saturated MOPS buffer at pH 7.0, $[O_2]$ = 230 μM [42]. The left panel (A) shows a narrower window of L-Trp concentrations (3 μM ⩽ [L-Trp] ⩽ 450 μM) and the right panel (B) displays the full range of [L-Trp] used in the study (3 μM ⩽ [L-Trp] ⩽ 5000 μM). Data represented by red circles were determined by O_2 depletion-based assays, $[h\text{IDO1}]_T$ = 219 nM. The error bars reflect ±σ from 3–5 individual experiments. The blue diamonds are from the NFK formation-based assays, where $[h\text{IDO1}]_T$ = 262 nM with 20 mM ascorbate, 10 μM methylene blue, and 100 U/mL catalase. The error bars reflect ±σ for 8–10 individual experiments. The solid lines are the best fits of the data to Eq. (1), and the dashed lines are the best fits to Eq. (2). (For interpretation of the references to color in this figure legend, the reader is referred to the web version of this article.)

fits of the data to Eqs. (1)–(3) were performed in KaleidaGraph 4.1 (Synergy Software).

Measurement of initial rates of hIDO1 catalysis by monitoring NFK appearance

The formation of NFK was continuously monitored by UV absorption at 321 nm using an Applied Photophysics SX-20 stopped-flow spectrophotometer with a thermostated drive-syringe compartment and fast kinetics observation cell (0.5 ms dead time, 0.2 cm optical path length). The instrument was interfaced to a computer workstation. The measurements were performed at air-saturation level of O_2 in 20 mM MOPS buffer at pH 7.0 and 25.0 °C. To eliminate interference from absorption of β-NADH at 340 nm ($\varepsilon = 6220\ M^{-1}\ cm^{-1}$) [45] during catalytic turnover, ascorbate/methylene blue reducing system was used instead of β-NADH/cytochrome b_5 reductase/cytochrome b_5. Typical final reactant concentrations were 20 mM for ascorbate and 10 μM for methylene blue; L-Trp was varied from 3 μM to 5000 μM; $[h\text{IDO1}]_T$ = 262 nM, and catalase was present at 100 U/mL. The reactions were initiated by combining ferric *h*IDO1 from one syringe of the stopped-flow instrument with the substrate/reductant mixture from the second syringe. Individual reactions were monitored for 50 s. Initial velocities of NFK formation (in μM/s) were determined in the range of the steepest linear increase of absorbance (~5 s long) at 321 nm ($\varepsilon_{NFK} = 3{,}750\ M^{-1}\ cm^{-1}$) [46], typically 2–4 s after mixing. Initial velocities were converted to specific activity of *h*IDO1 by dividing by micromolar $[h\text{IDO1}]_T$. The slopes and standard deviations were determined in Excel 2010 (Microsoft). All nonlinear fits of the data, shown in Fig. 1 by blue diamonds, were done in KaleidaGraph 4.1 (Synergy Software).

Results

Activity assay for hIDO1, based on O_2 consumption

Isolated *h*IDO1 exists in a ferric form and is inactive towards L-Trp dioxygenation. Ascorbate/methylene blue is a common activating system that reduces *h*IDO1 to a ferrous state [22–28]. Using these cofactors, the rate of NFK appearance can be monitored by absorption spectroscopy at 321 nm. Even though a single *h*IDO1 turnover is electroneutral, the presence of reductant is necessary to maintain the enzyme in its active ferrous form by outcompeting a facile *h*IDO1 autoxidation [38]. The ascorbate/methylene blue system performs well in air-saturated buffers [20]; however, at low O_2, significant oxygen consumption by the cofactors themselves [47] creates challenges for quantifying the effects of O_2 concentration on *h*IDO1 kinetics [26,47].

In order to avoid unproductive O_2 depletion, we employed a combination of cytochrome b_5 and cytochrome b_5 reductase for *in situ* activation of ferric *h*IDO1 with β-NADH [43]. Cu,Zn-SOD and catalase were also included in the assay mixture to eliminate trace amounts of possible byproducts of oxygen reduction: superoxide anion ($O_2^{\cdot-}$) and hydrogen peroxide (H_2O_2). It was proposed in the literature that cytochrome b_5 is an endogenous reductant for ferric *h*IDO1 *in vivo* [48,49]. Reducing systems, that include cytochrome b_5 and either cytochrome b_5 reductase and β-NADH or cytochrome P450 reductase and β-NADPH, have been previously utilized for *in vitro* activation of *h*IDO1 [33,50,51].

The initial rates of *h*IDO1 catalysis were determined at 25.0 °C in 20 mM MOPS buffer at pH 7.0 by continuous monitoring of O_2 levels with a Clark-type oxygen electrode. Representative O_2 concentration profiles obtained by this oxygen depletion-based assay are shown in Fig. S1 in the Supporting Information [41]. Individual experiments were conducted for 60–80 s. During this time, the reactions reached completion by exhausting either L-Trp or O_2. When reactions were limited by L-Trp, the O_2 consumption levels reached 92 ± 6% of a theoretical value based on the 1:1 stoichiometric relationship between L-Trp and O_2 (Scheme 1). Stable O_2 levels in the thermostated reaction chamber, recorded either prior to injection of ferric *h*IDO1 or upon reaction completion (as shown in Fig. S1A) [41], indicated insignificant O_2 disappearance in the absence of the enzyme and/or substrate and suggested that the extent of O_2-consuming side reactions in the assay mixture was negligible. When O_2 was a limiting reactant, its concentration dropped to near zero within 80 s (Fig. S1B) [41], indicating that *h*IDO1 maintained activity even at extremely low O_2. At elevated levels of L-Trp, O_2 disappearance was observable for minutes after the injection of *h*IDO1, until anaerobic conditions were reached in the reaction chamber (Fig. S1C) [41]. The rates of O_2 consumption were directly proportional to $[h\text{IDO1}]_T$ in the nM range of enzyme concentrations.

Since the postulated $O_2^{\cdot-}$ byproduct of *h*IDO1 autoxidation [6,38] could interfere with the rate of O_2 depletion (because of a very rapid dismutation by Cu,Zn-SOD that regenerates 0.5 mol of O_2 per 1.0 mol of $O_2^{\cdot-}$), we further validated the suitability of O_2 consumption-based protocol for studies of effects of O_2 concentration on *h*IDO1 catalysis. We compared the steady-state kinetic parameters obtained on a Clark-type oxygen electrode with those

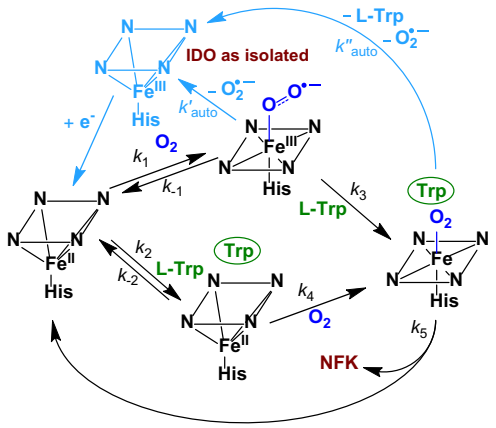

Scheme 2. Kinetic model for catalytic dioxygenation of L-Trp by *h*IDO1, used in our study. Adapted from Ref. [6]. The heme cofactor is shown as a parallelogram with nitrogen atoms at the corners; L-Trp, bound in the catalytic site of *h*IDO1, is indicated by an oval. Enzyme activation and the steps leading to deactivation of *h*IDO1 via autoxidation are shown in light blue. The catalytic steps are depicted in black. (For interpretation of the references to color in this figure legend, the reader is referred to the web version of this article.)

found via monitoring the appearance of NFK by stopped-flow techniques. We used a kinetic model, shown in Scheme 2, adapted from the published literature [6,23].

In Scheme 2, the reductive activation of the enzyme and two autoxidation steps (that deactivate *h*IDO1) are indicated by the light blue arrows. The catalytic steps are shown in black. The reduction of *h*IDO1 is very rapid. Upon injection of inactive ferric *h*IDO1, the enzyme is activated and steady-state is reached in 2–4 s, which is comparable to pre-steady-state kinetics of a fully reduced enzyme [26]. This allows us to write the material balance for the total concentration of *h*IDO1 during a steady-state catalytic turnover, supported by both reducing systems, as a sum of four catalytically-active forms, shown in Scheme 2 in black. These forms include a ternary complex – *h*IDO1·O_2·L-Trp, two binary complexes – $^{Fe(III)}$*h*IDO1·O_2^- and $^{Fe(II)}$*h*IDO1·L-Trp, and a free enzyme – $^{Fe(II)}$*h*IDO1. The half-life ($t_{1/2}$) of the binary $^{Fe(III)}$*h*IDO1·O_2^- complex in 20 mM MOPS at pH 7.0 and 20 °C, is ~100 s, indicating that this form undergoes autoxidation with $k'_{auto} = 0.006\ s^{-1}$ (Scheme 2) [38]. The rate constant for autoxidation of the ternary complex under the same conditions is significantly larger: $k''_{auto} = 0.17(2)\ s^{-1}$ (Scheme 2) [38]. However, as we show below, these processes do not significantly affect the steady-state kinetic parameters obtained by monitoring O_2 depletion.

Kinetics of hIDO1 in air-saturated buffer

In Fig. 1, the results of our O_2 consumption-based kinetic studies (red circles) are compared with those obtained by monitoring the appearance of NFK (blue diamonds).

Using the O_2 consumption-based assay at constant initial $[O_2] = 230\ \mu M$ and $[hIDO1]_T = 219\ nM$, rates were studied as a function of [L-Trp]. Substrate inhibition was observed as [L-Trp] was elevated from 3 μM to 400 μM (Fig. 1A, red circles) [22,23]. The data were fitted to Eq. (1), giving $^{Trp}k_{cat} = 8.2 \pm 0.3\ s^{-1}$, $^{Trp}K_M = 19 \pm 2\ \mu M$, and $^{Trp}K_{SI} = 296 \pm 34\ \mu M$:

$$\text{Initial Rate} = \frac{\frac{d[O_2]}{dt}}{[hIDO1]_T} = \frac{{}^{Trp}k_{cat}[L-Trp]}{{}^{Trp}K_M + [L-Trp]\left(1 + \frac{[L-Trp]}{{}^{Trp}K_{SI}}\right)} \quad (1)$$

Here, $^{Trp}k_{cat}$, $^{Trp}K_M$, and $^{Trp}K_{SI}$ are the apparent rate, Michaelis, and substrate inhibition constants, respectively; [L-Trp] is the concentration of varied inhibitory substrate: L-Trp [52]. Eq. (1) differs from the Michaelis–Menten equation by the presence of $\left(1 + \frac{[L-Trp]}{{}^{Trp}K_{SI}}\right)$ term in the denominator. When $[L-Trp] \gg {}^{Trp}K_{SI}$, this term dominates, reducing the right-hand side of Eq. (1) to $\frac{{}^{Trp}K_{SI}}{[L-Trp]} \times {}^{Trp}k_{cat}$. This demonstrates that the enzyme activity approaches zero as [L-Trp] is increased significantly above the $^{Trp}K_{SI}$. Eq. (1) is generally applicable to cases of complete substrate inhibition where continued growth in substrate concentration ultimately halts catalysis, causing characteristic non-hyperbolic behavior with a maximum rate observed at $[L-Trp] = \sqrt{{}^{Trp}K_M \times {}^{Trp}K_{SI}}$ [52].

Further increase in [L-Trp] beyond 400 μM suggests that observed substrate inhibition is partial rather than complete because initial rates appear to approach a plateau region at high [L-Trp] (Fig. 1B, red circles). Partial substrate inhibition often results from modifications of the catalytic pathway, rather than a complete loss of enzyme activity. Instead of Eqs. (1) and (2) is more suitable for fitting the data in cases of partial substrate inhibition [53]. Fitting the data, shown by red circles in Fig. 1B, to Eq. (2) gives $^{Trp}k_{cat} = 8.3 \pm 0.5\ \ s^{-1}$, $^{Trp}K_M = 19.0 \pm 2.7\ \mu M$, $^{Trp}K_{SI} = 200 \pm 42\ \mu M$, and $^{Trp}K'_{SI} = 1066 \pm 250\ \mu M$:

$$\text{Initial Rate} = \frac{-\frac{d[O_2]}{dt}}{[hIDO1]_T} = \frac{{}^{Trp}k_{cat}[L-Trp]\left(1 + \frac{[L-Trp]}{{}^{Trp}K'_{SI}}\right)}{{}^{Trp}K_M + [L-Trp]\left(1 + \frac{[L-Trp]}{{}^{Trp}K_{SI}}\right)} \quad (2)$$

Here, $^{Trp}k_{cat}$, $^{Trp}K_M$, $^{Trp}K_{SI}$ and [L-Trp] have the same meaning as in Eq. (1), and $^{Trp}K'_{SI}$ is another apparent substrate inhibition constant. If the value of $^{Trp}K'_{SI}$ is very large and $^{Trp}K'_{SI} \gg {}^{Trp}K_{SI}$, Eq. (2) reduces to Eq. (1), and the best fits of the data to Eqs. (2) and (1) become indistinguishable. Compared to Eq. (1), the numerator of Eq. (2) contains an extra term: $\left(1 + \frac{[L-Trp]}{{}^{Trp}K'_{SI}}\right)$. At high [L-Trp], the presence of this term reduces Eq. (2) to Initial Rate $= \frac{{}^{Trp}K_{SI}}{{}^{Trp}K'_{SI}} \times {}^{Trp}k_{cat}$, giving a constant non-zero value for the initial rate at high substrate concentration, hence the plateau region in Fig. 1B. The exact mathematical equations for expression of $^{Trp}k_{cat}$, $^{Trp}K_M$, $^{Trp}K_{SI}$, and $^{Trp}K'_{SI}$ (in terms of fixed $[O_2]$ and the rate constants for each elementary step) are dependent on the kinetic model under consideration. For the kinetic model used in our study (see Scheme 2), derivation of these expressions is shown in the Supporting Information [41].

Fitting the data, shown in Fig. 1A by the blue diamonds, to Eq. (1) gives $^{Trp}k_{cat} = 8.7 \pm 1.3\ s^{-1}$, $^{Trp}K_M = 28 \pm 8\ \mu M$, and $^{Trp}K_{SI} = 266 \pm 87\ \mu M$. These steady-state kinetic parameters, obtained by monitoring formation of NFK (Fig. 1), demonstrate similar dependence on the pH that was established for the rabbit enzyme [18,19]. It was previously reported that at pH 6.5 catalytic activity of *h*IDO1 is six times greater than at pH 8.0 [33]. At pH 8.0 [23], $^{Trp}k_{cat}$ was found to be $1.4 \pm 0.1\ s^{-1}$ and, at pH 7.4 [22], $^{Trp}k_{cat}$ was determined to be $3.1 \pm 0.2\ s^{-1}$. Thus, the value of $^{Trp}k_{cat} = 8.3\ s^{-1}$, reported here, may indicate that *h*IDO1 activity reaches a maximum at slightly acidic pH (between pH 6.5 and 7.0). The magnitudes of two other kinetic constants – $^{Trp}K_M$ and $^{Trp}K_{SI}$, also increase with decreasing pH. The Michaelis constant changes from 5.0 ± 0.3 μM at pH 8.0 to 15 ± 2 μM at pH 7.4 and ~30 μM at pH 7.0, while the substrate inhibition constant jumps from 65 ± 6 μM at pH 8.0 to 170 ± 20 μM at pH 7.4 and ~250 μM at pH 7.0 [22,23].

Fitting the data to Eq. (2), using the full range of L-Trp concentrations used in NFK-forming assays (Fig. 1B, blue diamonds), gives similar results to those obtained earlier by fitting the data in Fig. 1A (blue diamonds) to Eq. (1): $^{Trp}k_{cat} = 8.9 \pm 1.4\ s^{-1}$, $^{Trp}K_M = 29 \pm 9\ \mu M$, $^{Trp}K_{SI} = 174 \pm 68\ \mu M$, and $^{Trp}K'_{SI} = 1028 \pm 409\ \mu M$. Comparison of the steady-state kinetic parameters, obtained by monitoring depletion of O_2 with those obtained by observing the appearance of NFK, shows close agreement between these two

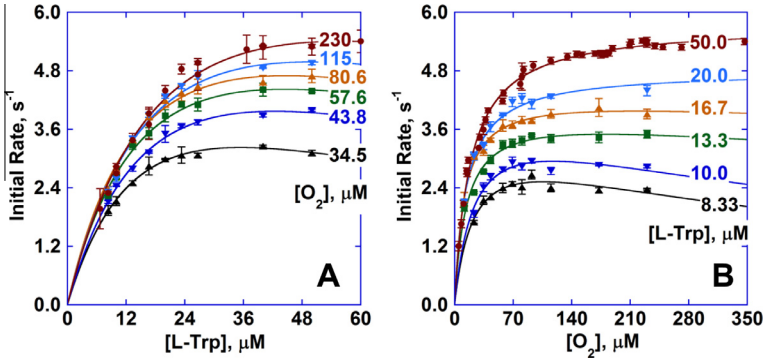

Fig. 2. Initial rates of *h*IDO1 catalysis, measured by monitoring O_2 depletion, in 20 mM MOPS buffer at pH 7.0 and 25.0 °C; $[hIDO1]_T$ = 188 nM, with the exception of the data shown by red circles where $[hIDO1]_T$ = 219 nM. (A) Fixed O_2 levels are indicated in the plot; L-Trp was varied from 8.33 μM to 50.0 μM. The solid lines show the best fits of the data to Eq. (1). (B) Fixed L-Trp levels are indicated in the plot; O_2 was varied from 11.5 μM to 230 μM; for 50.0 μM L-Trp, O_2 concentrations were changed from 4.6 μM to 348 μM. The solid lines are the best fits of the data to Eq. (3), except for 20.0 μM and 50.0 μM L-Trp where the Michaelis–Menten equation was used. The error bars reflect ±σ for 3–5 separate experiments. (For interpretation of the references to color in this figure legend, the reader is referred to the web version of this article.)

Table 1
Steady-state kinetic parameters – $^{Trp}k_{cat}$, $^{Trp}K_M$, $^{Trp}K_{SI}$, and $^{Trp}k_{cat}/K_M$ ratios, obtained by the best fit of the data in Fig. 2A to Eq. (1).

$[O_2]$ (μM)	$^{Trp}k_{cat}$ (s^{-1})	$^{Trp}K_M$ (μM)	$^{Trp}k_{cat}/K_M$[a] ($\mu M^{-1}\ s^{-1}$)	$^{Trp}K_{SI}$ (μM)
34.5	7.1 ± 0.9	21.1 ± 3.9	0.33 ± 0.08	59 ± 16
43.8	8.5 ± 1.1	24.0 ± 4.7	0.35 ± 0.08	75 ± 24
57.6	8.5 ± 1.5	20.7 ± 5.4	0.41 ± 0.13	95 ± 45
80.6	8.9 ± 1.8	20.1 ± 6.2	0.44 ± 0.16	100 ± 57
115	9.7 ± 2.7	23.4 ± 9.6	0.41 ± 0.20	104 ± 83
230	10.3 ± 1.5	25.6 ± 5.6	0.40 ± 0.11	124 ± 56
230[b]	8.3 ± 0.5	19.0 ± 2.7	0.44 ± 0.07	200 ± 42

[a] Here, $^{Trp}k_{cat}/K_M = {}^{Trp}k_{cat}/{}^{Trp}K_M$.
[b] From the best fit of the data, shown by red circles in Fig. 1B, to Eq. (2).

Table 2
Steady-state kinetic parameters – $^{O_2}k_{cat}$, $^{O_2}K_M$, $^{O_2}K_{SI}$, and $^{O_2}k_{cat}/K_M$ ratios, derived from the best fit of the data in Fig. 2B to Eq. (3).

[L-Trp] (μM)	$^{O_2}k_{cat}$ (s^{-1})	$^{O_2}K_M$ (μM)	$^{O_2}k_{cat}/K_M$[a] ($\mu M^{-1}\ s^{-1}$)	$^{O_2}K_{SI}$ (μM)
8.33	3.7 ± 0.4	23.7 ± 6.4	0.15 ± 0.04	468 ± 175
10.0	4.2 ± 0.4	24.0 ± 6.2	0.17 ± 0.05	572 ± 234
13.3	4.1 ± 0.2	14.2 ± 2.3	0.28 ± 0.05	2270 ± 1635
16.7	4.4 ± 0.1	11.5 ± 1.2	0.38 ± 0.04	4101 ± 2974
20.0[b]	4.8 ± 0.1	14.0 ± 1.2	0.34 ± 0.03	–
50.0[b]	5.8 ± 0.1	18.6 ± 0.6	0.31 ± 0.01	–

[a] Here, $^{O_2}k_{cat}/K_M = {}^{O_2}k_{cat}/{}^{O_2}K_M$.
[b] From the best fit to the Michaelis–Menten equation.

assays. Within experimental error, the steady-state kinetic parameters are identical.

Steady-state kinetics of hIDO1 at low O_2

We examined steady-state kinetics of *h*IDO1 by monitoring O_2 depletion. The concentration of one substrate was varied, while the second substrate was held constant at several sub-saturation levels [54]. From our saturation kinetics studies described above, the near-maximum activity of *h*IDO1 was observed at ~50 μM L-Trp and ~230 μM O_2. Treating O_2 as a fixed substrate, we systematically lowered its initial concentration, measuring rates of *h*IDO1 catalysis for each level as a function of [L-Trp]. In these experiments, [L-Trp] was varied from 8.33 μM to 50.0 μM at six fixed levels of O_2 from 34.5 μM to 230 μM (Fig. 2A). Similarly, in a separate set of experiments, $[O_2]$ was varied from 11.5 μM to 230 μM at six fixed levels of L-Trp between 8.33 μM and 50.0 μM (Fig. 2B). For both substrates, these levels cover the physiological ranges of O_2 and L-Trp concentrations [17,36,37] and bracket the values for apparent $^{Trp}K_M$ and $^{O_2}K_M$ that are near ~20 μM (Tables 1 and 2).

The best fit of the data in Fig. 2A to Eq. (1) yields the steady-state kinetic parameters – $^{Trp}k_{cat}$, $^{Trp}K_M$, and $^{Trp}K_{SI}$, which are shown in Table 1. The $^{Trp}k_{cat}/K_M$ ratios, calculated with errors propagated from uncertainties in the fitted values of $^{Trp}k_{cat}$ and $^{Trp}K_M$, are also summarized in Table 1. These ratios represent an apparent second-order rate constant for the reaction of *h*IDO1 and L-Trp to form NFK, and provide a measure of enzyme catalytic efficiency for each fixed $[O_2]$. Similarly, the values of $^{O_2}k_{cat}$, $^{O_2}K_M$, and $^{O_2}K_{SI}$, obtained by the best fit of the data in Fig. 2B to Eq. (3), are given in Table 2 together with the calculated $^{O_2}k_{cat}/K_M$ ratios. In this case, the $^{O_2}k_{cat}/K_M$ ratios correspond to an apparent second-order rate constant for the reaction of *h*IDO1 with O_2 to form NFK at each fixed level of L-Trp. The uncertainty in the magnitude of $^{O_2}k_{cat}/K_M$ is significantly smaller than that of $^{Trp}k_{cat}/K_M$, which is a consequence of smaller experimental errors in both $^{O_2}k_{cat}$ and $^{O_2}K_M$, compared to the errors in $^{Trp}k_{cat}$ and $^{Trp}K_M$.

$$\text{Initial Rate} = \frac{-\frac{d[O_2]}{dt}}{[hIDO1]_T} = \frac{{}^{O_2}k_{cat}[O_2]}{{}^{O_2}K_M + [O_2]\left(1 + \frac{[O_2]}{{}^{O_2}K_{SI}}\right)} \quad (3)$$

Here, $^{O_2}k_{cat}$, $^{O_2}K_M$, and $^{O_2}K_{SI}$ are the apparent rate, Michaelis, and substrate inhibition constants, respectively; $[O_2]$ is the concentration of varied inhibitory substrate – O_2. Eq. (3) is identical to Eq. (1), except here the roles of the substrates are switched and substrate inhibition is observed with varied O_2 at fixed L-Trp [52].

Varying $[O_2]$ at constant [L-Trp] = 50.0 μM (the value that gives near-maximum velocity at air-saturation) results in typical saturation kinetics (Fig. 2B) with $^{O_2}k_{cat}$ = 5.8 ± 0.1 s^{-1} and $^{O_2}K_M$ = 18.6 ± 0.6 μM. This value of $^{O_2}K_M$ is lower than a typical physiological level of O_2 in tissues, which ranges from ~35 μM to ~65 μM [17]. It is also somewhat lower than that reported at pH 7.4 ($^{O_2}K_M$ = 42 μM) [22] or estimated at pH 8.0 ($^{O_2}K_M$ < 50 μM) [26].

The dependence of $^{Varied}k_{cat}/K_M$ for varied substrate on the concentration of fixed substrate signals sequential addition of O_2 and L-Trp to *h*IDO1 (Fig. 3). A straight line in a double reciprocal plot, such as 1/(Initial Rate) vs. 1/[Varied], has a slope that is a reciprocal of $^{Varied}k_{cat}/K_M$. Thus, independence of $^{Varied}k_{cat}/K_M$ on the level of fixed substrate is algebraically equivalent to a set of parallel lines in the double reciprocal plot, which is indicative of a ping-pong mechanism [52]. Therefore, seeing an increase in the value of $^{O_2}k_{cat}/K_M$ with rising concentration of L-Trp (Fig. 3, blue diamonds) favors a sequential kinetic mechanism. This mechanism

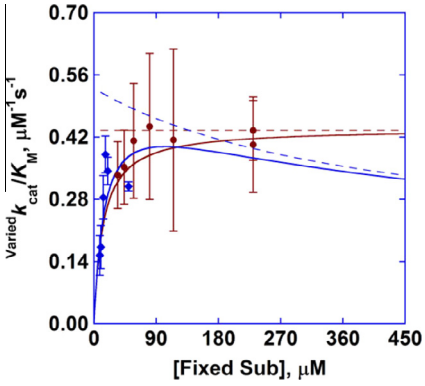

Fig. 3. Dependence of the $^{Varied}k_{cat}/K_M$ ratios on the initial concentration of fixed substrate. The data are from Tables 1 and 2. The red circles and red lines correspond to $^{Trp}k_{cat}/K_M$ vs. fixed [O_2], while the blue diamonds and blue lines depict $^{O_2}k_{cat}/K_M$ vs. fixed [L-Trp]. The error bars reflect propagated experimental uncertainty in the values of k_{cat} and K_M. The solid and dashed lines show the $^{Varied}k_{cat}/K_M$ ratios, modeled using Eqs. (6) (red) and (9) (blue). The dashed lines correspond to the model with $k_{-1} = 0\ s^{-1}$. (For interpretation of the references to color in this figure legend, the reader is referred to the web version of this article.)

requires the presence of both substrates in the catalytic site of *h*IDO1 before NFK can be formed and released. Furthermore, since the sequential entry of substrates into the catalytic cycle also requires a reversible process, which links the two substrate-bound enzyme forms, binding of the first substrate to *h*IDO1 must be reversible. The values of $^{Trp}k_{cat}/K_M$ appear to be independent of the concentration of fixed O_2 substrate (Fig. 3, red); this, however, does not rule out the mechanism depicted in Scheme 2. As can be seen from our modeling results, shown by solid and dashed lines in Fig. 3, the $^{Trp}k_{cat}/K_M$ is expected to either be a constant (dashed line) or rapidly ascend to a plateau region with rising O_2 (solid line), depending on the kinetic model. The details of modeling studies are discussed below.

Modeling the dependence of $^{Varied}k_{cat}/K_M$ on concentrations of fixed substrate

The availability of the individual rate constants (shown in the catalytic portion of Scheme 2), in the published literature and current study, allows for the modeling of $^{Varied}k_{cat}/K_M$ ratios, whose experimental values are given in Tables 1 and 2. Raven and co-workers measured previously unreported rate constants for binding and dissociation of O_2 to and from ferrous *h*IDO1: $k_1 = (5.3 \pm 0.06) \times 10^5\ M^{-1}\ s^{-1}$ and $k_{-1} = 6.8 \pm 1.8\ s^{-1}$ (Scheme 2) [26]. Very recently, Nienhaus and co-workers determined a unimolecular rate constant for dissociation of L-Trp from a complex of ferrous *h*IDO1 with carbon monoxide and L-Trp, abbreviated here as $^{Fe(II)}$*h*IDO1·CO·L-Trp [35]. The authors used the value of the constant as an estimate for the dissociation constant of L-Trp from $^{Fe(II)}$*h*IDO1·L-Trp complex, $k_{-2} = 501 \pm 10\ s^{-1}$ (Scheme 2) [35]. They also calculated the value of k_2 as $1.25 \times 10^6\ M^{-1}\ s^{-1}$ from k_{-2} and $^{Trp}K_d = 400 \pm 70\ \mu M$ [55] (an equilibrium constant for dissociation of L-Trp from $^{Fe(II)}$*h*IDO1·L-Trp). The magnitude of k_3 (Scheme 2) can be estimated from $^{Trp}k_{cat}/K_M$ ratio measured at a high level of O_2, where $k_1[O_2] \gg k_{-1}$. It can be seen from Scheme 2 that a high level of oxygen makes the first step (addition of O_2 to ferrous *h*IDO1) kinetically irreversible with $k_{-1} = 0$, reducing Eq. (6) (shown below) to $^{Trp}k_{cat}/K_M = k_3$ [23,56]. From the fit of the data, obtained at air saturation ([O_2] = 230 μM) and displayed as red circles in Fig. 1B, to Eq. (2), we obtained $^{Trp}k_{cat} = 8.3 \pm 0.5\ s^{-1}$ and $^{Trp}K_M = 19.0 \pm 2.7\ \mu M$. The ratio of these constants gives the value of $k_3 = (4.37 \pm 0.74) \times 10^5\ M^{-1}\ s^{-1}$, which is in agreement with the $k_{on} = (1.2 \pm 0.1) \times 10^5\ M^{-1}\ s^{-1}$ reported by

Table 3
Steady-state constants – $^{Trp}k_{cat}$ and $^{Trp}K_M$, and $^{Trp}k_{cat}/K_M$ ratios, calculated using Eqs. (4)–(6).

[O_2] (μM)	$^{Trp}k_{cat}$ (s^{-1})	$^{Trp}K_M$ (μM)	$^{Trp}k_{cat}/K_M$[a] ($\mu M^{-1}\ s^{-1}$)
34.5	5.6	17.6	0.32
43.8	6.1	17.8	0.34
57.6	6.5	18.0	0.36
80.6	6.9	18.2	0.38
115	7.3	18.3	0.40
230	7.7	18.5	0.42

[a] Here, $^{Trp}k_{cat}/K_M = {}^{Trp}k_{cat}/{}^{Trp}K_M$.

Yeh and co-workers for the binding of L-Trp to a complex of ferric *h*IDO1 with cyanide anion – $^{Fe(III)}$*h*IDO1·CN^-, which authors used as a mimic of the ferrous *h*IDO1 adduct with O_2 – $^{Fe(III)}$*h*IDO1·O_2^- [55]. Using stopped-flow to monitor absorbance at 570 nm, Raven and co-workers measured the rate of oxygen binding to ferrous *h*IDO1 in the presence of L-Trp, $k_4 = (1.6 \pm 0.2) \times 10^5\ M^{-1}\ s^{-1}$ (Scheme 2) [23]. The value of k_5 can be approximated by $^{Trp}k_{cat}$, measured at high O_2. Similarly to Eqs. (6) and (4) can be greatly simplified when $k_1[O_2] \gg k_{-1}$. In this case, k_{-1} is effectively zero, and Eq. (4) reduces to $^{Trp}k_{cat} = k_5$; thus, $k_5 = 8.3 \pm 0.5\ s^{-1}$ [57]. Using these values of the rate constants, we calculated the magnitude of $^{Trp}k_{cat}$, $^{Trp}K_M$, and $^{Trp}k_{cat}/K_M$ (Table 3) and $^{O_2}k_{cat}$, $^{O_2}K_M$, and $^{O_2}k_{cat}/K_M$ (Table 4) for several levels of fixed substrate, using Eqs. (4)–(9), respectively [58]. The calculated values of $^{Trp}k_{cat}/K_M$ and $^{O_2}k_{cat}/K_M$ are plotted in Fig. 3 as solid lines. The results of modeling predict that the $^{Varied}k_{cat}/K_M$ ratio is dependent on the level of fixed substrate, characteristic of a sequential kinetic mechanism [52]. Good agreement between the experimental and computed values (Fig. 3) offers support for the use of the catalytic cycle, depicted in Scheme 2, for describing the kinetic mechanism of *h*IDO1.

$$^{Trp}k_{cat} = \frac{k_4[O_2] + k_{-2} + \frac{\alpha}{\beta}k_{-1}}{\left(\frac{1}{k_1[O_2]} + \frac{1}{k_5}\right)\left(k_4[O_2] + k_{-2} + \frac{\alpha}{\beta}k_{-1}\right) + \frac{1-\alpha}{\beta} \times \frac{k_{-1}}{k_1[O_2]}} \quad (4)$$

$$^{Trp}K_M = \frac{\frac{1}{k_3}(k_4[O_2] + k_{-2})\left(1 + \frac{k_{-1}}{k_1[O_2]}\right)}{\left(\frac{1}{k_1[O_2]} + \frac{1}{k_5}\right)\left(k_4[O_2] + k_{-2} + \frac{\alpha}{\beta}k_{-1}\right) + \frac{1-\alpha}{\beta} \times \frac{k_{-1}}{k_1[O_2]}} \quad (5)$$

$$^{Trp}k_{cat}/K_M = \frac{^{Trp}k_{cat}}{^{Trp}K_M} = \frac{k_3\left(k_4[O_2] + k_{-2} + \frac{\alpha}{\beta}k_{-1}\right)}{(k_4[O_2] + k_{-2})\left(1 + \frac{k_{-1}}{k_1[O_2]}\right)} \quad (6)$$

$$^{O_2}k_{cat} = \frac{\alpha k_2[\text{L-Trp}] + k_{-2} + \frac{\alpha}{\beta}k_{-1}}{\left(\frac{1}{k_3[\text{L-Trp}]} + \frac{1}{k_5}\right)\left(\alpha k_2[\text{L-Trp}] + k_{-2} + \frac{\alpha}{\beta}k_{-1}\right) + \alpha\left(1 - \frac{1}{\beta}\right)} \quad (7)$$

$$^{O_2}K_M = \frac{\frac{1}{k_1}(k_2[\text{L-Trp}] + k_{-2})\left(1 + \frac{k_{-1}}{k_3[\text{L-Trp}]}\right)}{\left(\frac{1}{k_3[\text{L-Trp}]} + \frac{1}{k_5}\right)\left(\alpha k_2[\text{L-Trp}] + k_{-2} + \frac{\alpha}{\beta}k_{-1}\right) + \alpha\left(1 - \frac{1}{\beta}\right)} \quad (8)$$

$$^{O_2}k_{cat}/K_M = \frac{^{O_2}k_{cat}}{^{O_2}K_M} = \frac{k_1\left(\alpha k_2[\text{L-Trp}] + k_{-2} + \frac{\alpha}{\beta}k_{-1}\right)}{(k_2[\text{L-Trp}] + k_{-2})\left(1 + \frac{k_{-1}}{k_3[\text{L-Trp}]}\right)} \quad (9)$$

Here, k_1, k_{-1}, k_2, k_{-2}, k_3, k_4, and k_5 are the individual rate constants (Scheme 2); $\alpha = k_4/k_1$ and $\beta = k_3/k_2$. [O_2] and [L-Trp] are the initial concentrations of substrates.

The dashed lines in Fig. 3 show the results of modeling the $^{Trp}k_{cat}/K_M$ (red) and $^{O_2}k_{cat}/K_M$ (blue) ratios, assuming that the addition of O_2 to free $^{Fe(II)}$*h*IDO1 is irreversible with $k_{-1} = 0\ s^{-1}$ (Scheme 2) [23]. Such an assumption is most valid at high O_2, where $k_1[O_2] \gg k_{-1}$ and the dashed and solid lines begin to merge

Table 4
Steady-state constants – $^{O_2}k_{cat}$ and $^{O_2}K_M$, and $^{O_2}k_{cat}/K_M$ ratios, calculated using Eqs. (7)–(9).

[L-Trp] (μM)	$^{O_2}k_{cat}$ (s^{-1})	$^{O_2}K_M$ (μM)	$^{O_2}k_{cat}/K_M$[a] ($\mu M^{-1}\ s^{-1}$)
8.33	2.5	13.7	0.19
10.0	2.9	13.9	0.21
13.3	3.4	14.2	0.24
16.7	3.9	14.4	0.27
20.0	4.3	14.6	0.29
50.0	6.0	16.0	0.38

[a] Here, $^{O_2}k_{cat}/K_M = {}^{O_2}k_{cat}/{}^{O_2}K_M$.

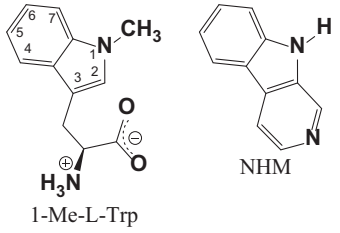

Scheme 3. Substrate analogs of L-Trp and O_2, respectively, used in *h*IDO1 inhibition studies.

(Fig. 3). However, at low O_2, the reversibility of the first step is essential for accurate reproduction of experimental $^{O_2}k_{cat}/K_M$ ratios (Fig. 3, blue diamonds).

Kinetics of hIDO1 in the presence of substrate analogs

To support the use of the kinetic model shown in Scheme 2 for describing the mechanism of catalytic dioxygenation of L-Trp, we studied the inhibition patterns in the presence of two substrate analogs – 1-methyl-L-tryptophan (1-Me-L-Trp) and norharmane (NHM), shown in Scheme 3.

Using binding studies by means of optical absorption and CD spectroscopy, it was shown in the literature that 1-Me-L-Trp binds to the active site of IDO in a manner very similar to that of L-Trp [59]. In *h*IDO1, 1-Me-L-Trp is a competitive inhibitor versus L-Trp [22,60]. When, however, 1-Me-L-Trp is the only indoleamine in the reaction mixture it is a very slow substrate for *h*IDO1 [60]. Even though the dioxygenation of 1-Me-L-Trp is slow, its occurrence suggests that the binding of 1-Me-L-Trp to the catalytic site of *h*IDO1 does not completely impede the interactions that normally occur between O_2 and the enzyme, with the organic substrate bound near the heme moiety.

Sono demonstrated that in the rabbit enzyme, NHM is a noncompetitive inhibitor versus L-Trp [47]. The authors showed (1) that NHM binds to the ferrous catalytically-active form (by coordinating the heme iron center through the nitrogen atom of the pyridine moiety in NHM) with only a slightly negative cooperative effect on the binding of L-Trp and (2) that NHM directly competes with O_2 for the ferrous heme center [47]. We performed spectrophotometric titration of ferric *h*IDO1 with NHM to compare the inhibitor's binding in *h*IDO1 with that in the rabbit enzyme (Figs. S2 and S3) [41]. Similarities in the optical changes upon titration of *h*IDO1 with NHM, and in the values of $^{NHM}K_d$ found for *h*IDO1 and the rabbit enzyme, indicate that NHM binding is identical for both human and rabbit enzymes (Figs. S2 and S3) [41].

We used 1-Me-L-Trp and NHM as the analogs of L-Trp and O_2, respectively. According to the mechanism in Scheme 2, 1-Me-L-Trp is expected to bind to the free enzyme form and its binary complex with O_2 – $^{Fe(III)}$*h*IDO1·O_2^-, the same two forms that interact with L-Trp; while, NHM should be able to form complexes with both forms of *h*IDO1 that bind oxygen, the free enzyme and its binary complex with L-Trp – $^{Fe(II)}$*h*IDO1·L-Trp. The inhibition patterns that could be expected for a particular bi-substrate mechanism were summarized by Fromm [61]. Rules for predicting such patterns were developed by Cook and Cleland [62]. For a sequential random mechanism, as the one shown in Scheme 2, which can be either rapid equilibrium or steady-state, the inhibition patterns are expected to be similar for both substrate analogs. A competitive inhibition pattern is expected when the varied substrate is a match for the substrate analog. A net noncompetitive pattern is predicted for the mismatching varied substrate [61,62].

Inhibition patterns for 1-Me-L-Trp and NHM were obtained at sub-saturating concentrations of fixed substrate to prevent any distortion due to *h*IDO1 saturation [61]. At fixed O_2, L-Trp was varied from 10.0 to 23.3 μM and initial velocities were measured in the absence and presence of added substrate-analog inhibitors. Similar experiments were performed at constant L-Trp, where [O_2] was varied from 34.5 to 57.6 μM. With O_2 as a fixed substrate, its concentration was 46.1 μM; while with constant L-Trp, its level was kept at 16.7 μM. Double reciprocal plots (Fig. 4) show that 1-Me-L-Trp is a competitive inhibitor for L-Trp ($K_i = 5.2 \pm 0.3$ μM) and a noncompetitive inhibitor for O_2 ($K_i = 5.2 \pm 0.8$ μM), while NHM is a competitive inhibitor for O_2 ($K_i = 12 \pm 7$ μM) and a noncompetitive inhibitor for L-Trp ($K_i = 30 \pm 16$ μM). Replots of the data in Fig. 4C and D, by the method of Cornish-Bowden [63], lead to unmistakable assignments of NHM as a competitive inhibitor versus O_2, and of 1-Me-L-Trp as a noncompetitive one versus O_2 (Fig. S4) [41].

Fig. 4 illustrates that 1-Me-L-Trp, a competitive inhibitor versus L-Trp (Fig. 4A), is a noncompetitive one versus O_2 (Fig. 4C and also Fig. S4B). Furthermore, NHM, which is a competitive inhibitor versus varied O_2 (Fig. 4D and also Fig. S4A), is also a noncompetitive inhibitor versus varied L-Trp (Fig. 4B). Such a symmetric inhibition pattern, observed for both substrate analogs, validates the kinetic model used in our study (Scheme 2) [61,62]. For either an ordered or ping-pong kinetic mechanism, the inhibition pattern would have been uncompetitive for either one or both mismatching pairs of varied substrate/substrate analog, respectively [61,62].

Discussion

A typical total [L-Trp], comprising the free and albumin-bound forms, in the circulatory system of healthy blood donors is 73 ± 15 μM [36]. Tissue concentration of L-Trp measured in rats varies from ~20% (brain) to ~180% (liver) of the total L-Trp serum level [37]. If the tissue distribution of L-Trp in humans is similar, then the physiological levels of L-Trp are expected to vary from ~14 μM to ~130 μM. Maximum catalytic activity of *h*IDO1 in air-saturated buffer is observed at [L-Trp] ≈ 73 μM (Fig. 1A). As O_2 concentration drops to the levels of normal tissue oxygenation [17], the L-Trp concentration, which gives the maximum catalytic rate, appears to drop to 35 ± 12 μM (Fig. 2A, black line), suggesting that at physiological levels of both substrates, catalytic activity of *h*IDO1 is modulated by L-Trp. In the following discussion we propose a kinetic mechanism for such modulation of *h*IDO1 catalytic activity by L-Trp.

Kinetic mechanism of hIDO1 catalysis

A good agreement among the experimentally-obtained $^{Trp}k_{cat}/K_M$ and $^{O_2}k_{cat}/K_M$ ratios and their computed values (modeled using the catalytic steps in Scheme 2), indicates that the reversibility of O_2 binding to ferrous *h*IDO1 is impacting the catalytic efficiency of the enzyme at low O_2. The computed $^{Trp}k_{cat}/K_M$ and $^{O_2}k_{cat}/K_M$ ratios are represented by the solid lines in Fig. 3. A kinetic model

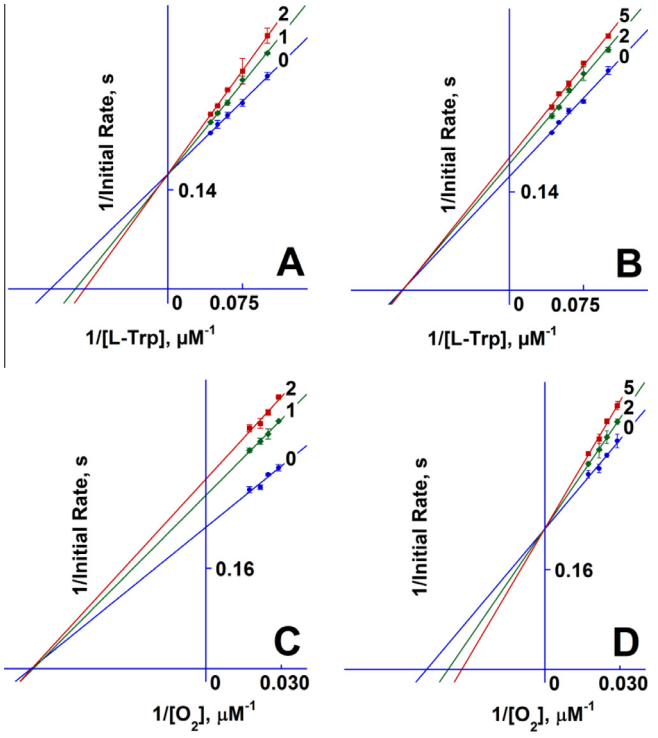

Fig. 4. Double-reciprocal plots, 1/initial rate vs. 1/[L-Trp] and 1/initial rate vs. $1/[O_2]$, showing *h*IDO1 inhibition patterns for 1-Me-L-Trp (A and C) and norharmane (B and D); the error bars reflect ±σ for 3–5 individual experiments; the solid lines are the best linear fits of the data, extrapolated to axis limits; fixed μM inhibitor concentrations are shown on the lines. Here, $[hIDO1]_T$ ranges from 160 nM to 188 nM. A and B: varied [L-Trp], fixed $[O_2]$ = 46.1 μM. C and D: varied $[O_2]$, fixed [L-Trp] = 16.7 μM.

that does not take into account the reversibility of O_2 binding in Step 1 (dashed lines in Fig. 3) overestimates the magnitude of ${}^{O_2}k_{cat}/K_M$

Even though Steps 1 and 2 in Scheme 2 are reversible, the existence of a rapid pre-equilibrium for binding of substrate to the free enzyme is not assured. A distinction between the steady-state and rapid pre-equilibrium mechanisms can be made by comparing the dissociation rate constants – k_{-1} and k_{-2} (Scheme 2), with the values of ${}^{Trp}k_{cat}$ and ${}^{O_2}k_{cat}$. When the off rate constants for O_2 from ${}^{Fe(III)}$*h*IDO1·O_2^- and L-Trp from ${}^{Fe(II)}$*h*IDO1·L-Trp do not greatly exceed the values of ${}^{Trp}k_{cat}$ and ${}^{O_2}k_{cat}$, a steady-state mechanism is operational rather than a rapid pre-equilibrium one [64,65]. Since the value of k_{-2} = 501±10 s^{-1} (Scheme 2) [35] is significantly greater than ${}^{Trp}k_{cat}$ or ${}^{O_2}k_{cat}$, the binding of L-Trp to ferrous *h*IDO1 is expected to always be at equilibrium. However, the value of k_{-1} = 6.8 ± 1.8 s^{-1} (Scheme 2) is comparable to k_{cat} = 1.4 ± 0.05 s^{-1} at pH 8.0 [26], and smaller than ${}^{Trp}k_{cat}$ = 8.3 ± 0.5 s^{-1} found in the current study [66], supporting a steady-state regime for binding of O_2 to ${}^{Fe(II)}$*h*IDO1 [64]. Subsequently, the steady-state concentrations of O_2, ${}^{Fe(II)}$*h*IDO1, and ${}^{Fe(III)}$*h*IDO1·O_2^- are not at equilibrium. Such nonequilibrium distribution of the active forms of the enzyme could lead to nonhyperbolic curves in plots of initial rates versus varied substrate concentration, if the pathways (from ${}^{Fe(II)}$*h*IDO1 to the ternary complex in Scheme 2) differ significantly in rate [67,68]. This unusual kinetic behavior highlights the fact that apparent enzyme inhibition does not have to involve more than one substrate binding site or more than one substrate molecule bound to the enzyme [67]. It is worth noting here that this effect vanishes in systems where all the active forms of the enzyme are at equilibrium [67].

When the concentration of one of the substrates for a bi-substrate enzyme is varied (substrate A), while the other substrate is fixed (substrate B), a general form of the steady-state initial rate expression is represented by Eq. (10) [65,67].

$$\text{Initial Rate} = \frac{i[A]^2 + j[A]}{k + l[A]^2 + m[A]} \tag{10}$$

Here, [*A*] is the concentration of varied substrate *A*, and *i*, *j*, *k*, *l*, and *m* are the products of the concentration of fixed substrate *B* and a combination of rate constants for various steps within the kinetic model [65,67]. The exact form of expressions for *i*, *j*, *k*, *l*, and *m* as a function of the individual rate constants and [*B*] could be quite complex. Ferdinand has demonstrated, by double differentiation of Eq. (10), that when $i \times m < j \times l$ and $i \times k < j \times m$, the initial rate curve (for varied substrate *A* at constant substrate *B*) shows an apparent enzyme inhibition at high levels of *A* [67].

L-Trp is a strong inhibitory substrate for *h*IDO1. Eq. (2) describes the dependence of the initial rate of *h*IDO1 catalysis on [L-Trp]. Eq. (10) can be recast as Eq. (2) by applying the following substitutions: $i = {}^{Trp}k_{cat}/{}^{Trp}K'_{SI}$, $j = {}^{Trp}k_{cat}$, $k = {}^{Trp}K_M$, $l = 1/{}^{Trp}K_{SI}$, and $m = 1$. Using the values of the steady-state kinetic parameters found by fitting the data, shown by red circles in Fig. 1B, to Eq. (2) (${}^{Trp}k_{cat}$ = 8.3 ± 0.5 s^{-1}, ${}^{Trp}K_M$ = 19.0 ± 2.7 μM, ${}^{Trp}K_{SI}$ = 200 ± 42 μM, and ${}^{Trp}K'_{SI}$ = 1066 ± 250 μM), we obtain the values of constants in Eq. (10): *i* = 0.008 ± 0.002 μM^{-1} s^{-1}, *j* = 8.3 ± 0.5 s^{-1}, *k* = 19.0 ± 2.7 μM, *l* = 0.005 ± 0.001 μM^{-1}, and *m* = 1. These constants satisfy the conditions of Ferdinand [67]: $i \times m$ = 0.008 ± 0.002 μM^{-1} s^{-1} < $j \times l$ = 0.042 ± 0.024 μM^{-1} s^{-1} and $i \times k$ = 0.152 ± 0.125 s^{-1} < $j \times m$ = 8.3 ± 0.5 s^{-1}. Thus, the description of the inhibition of *h*IDO1 by L-Trp, in terms of only one binding site that accepts only one molecule of L-Trp during the turnover, does not contradict the kinetic model shown in Scheme 2.

Inhibition of hIDO1 by L-Trp

Three recent studies addressed the origin of L-Trp inhibition of *h*IDO1 [22,23,35]. The activity of the enzyme was proposed to be inhibited at high level of L-Trp due to (a) the presence of a second inhibitory site [22], which binds L-Trp only weakly (hence the requirement for high L-Trp concentration), reducing the affinity of the catalytic site for L-Trp, (b) the lowering of k_4 relative to k_1 (Scheme 2) upon binding of L-Trp to a single active site as a result of an increase in heme redox potential [23], or (c) the dead-end inhibition by L-Trp that reversibly binds to ${}^{Fe(II)}$*h*IDO1, forming an inactive binary complex – ${}^{Fe(II)}$*h*IDO1·L-Trp [35].

A steady-state mechanistic model (Scheme 2), where one path from ${}^{Fe(II)}$*h*IDO1 to the ternary complex is preferred, provides a rationale for inhibition of *h*IDO1 by L-Trp that involves only one binding site and one molecule of L-Trp [23,67,68]. The magnitude of ${}^{Trp}K'_{SI}$, given by Eq. (11) [69], becomes a convenient reference point for analysis of the inhibitory effects of L-Trp.

$${}^{Trp}K'_{SI} = \frac{1}{\alpha}\left(\frac{k_4[O_2] + k_{-2}}{k_2}\right) + \frac{k_{-1}}{k_3} \tag{11}$$

Here, k_{-1}, k_2, k_{-2}, k_3, and k_4 are the individual rate constants shown in Scheme 2 and $\alpha = k_4/k_1$. When the concentration of L-Trp is approximately equal to ${}^{Trp}K'_{SI}$, the rates of O_2 depletion/NFK formation, via the top and the bottom pathways in Scheme 2, are equal. Eq. (S37) in the Supporting information illustrates this point [41]. At [L-Trp] ≈ ${}^{Trp}K'_{SI}$, both pathways in Scheme 2 contribute equally to formation of the ternary complex – *h*IDO1·O_2·L-Trp, which disappears at twice the rate of individual pathways. For a fixed level of O_2 (such as air-saturation level), when [L-Trp] ≪ ${}^{Trp}K'_{SI}$, the top pathway in Scheme 2 dominates over the bottom route, because at low level of L-Trp, nearly

irreversible addition of O_2 elevates $k_1[O_2]$ over k_2[L-Trp], even though $k_2 > k_1$. As [L-Trp] rises, the rate of the top pathway accelerates due to an increase in k_3[L-Trp][$^{Fe(III)}$*h*IDO1·O_2^-] term, resulting in greater overall velocity. However, as concentration of L-Trp increases, so does the contribution of the slower pathway to the total rate, which leads to an apparent inhibition of the rate of O_2 depletion/NFK formation. The overall velocity passes through a maximum [67,68]. In air-saturated buffer solution, maximum activity of *h*IDO1 is observed at [L-Trp] ≈ 73 μM (Fig. 1A). At this level of L-Trp, the bottom path to the ternary complex in Scheme 2 contributes ~6% of the overall rate (see Eq. (S35) in the Supporting information). The rise in [L-Trp] beyond 73 μM increases contribution of the bottom pathway, inhibiting the overall process. When [L-Trp] ≫ $^{Trp}K'_{SI}$, the initial rate reaches a plateau where the bottom pathway dominates (Scheme 2). For example, at 5 mM level of L-Trp, the contribution of this pathway is ~78%, and at 10 mM it reaches ~88% [41].

Modeling inhibition of hIDO1 by L-Trp

The initial rate of catalysis, obtained by varying L-Trp at a fixed O_2 level at air-saturation, is inhibited as L-Trp concentration increases (red circles in Fig. 1B). We modeled L-Trp inhibition of *h*IDO1 using Eq. (12), which describes initial rate of oxygen consumption as a function of initial substrate concentrations and the individual rate constants for the catalytic steps in Scheme 2 [70]:

$$\frac{-\frac{d[O_2]}{dt}}{[hIDO1]_T} = \frac{1 - \frac{k_{-1}}{k_1[O_2]} \times \frac{k_1[O_2]}{k_3[L\text{-}Trp]+k_{-1}} + \alpha \times \frac{k_2[L\text{-}Trp]}{k_4[O_2]+k_{-2}}}{\frac{1}{k_1[O_2]}\left(1 + \frac{k_1[O_2]}{k_3[L\text{-}Trp]+k_{-1}} + \frac{k_2[L\text{-}Trp]}{k_4[O_2]+k_{-2}} + \frac{k_3[L\text{-}Trp]}{k_5} \times \frac{k_1[O_2]}{k_3[L\text{-}Trp]+k_{-1}} + \frac{k_4[O_2]}{k_5} \times \frac{k_2[L\text{-}Trp]}{k_4[O_2]+k_{-2}}\right)} \quad (12)$$

Here, k_1, k_{-1}, k_2, k_{-2}, k_3, k_4, and k_5 are the rate constants for the catalytic steps, shown in black in Scheme 2; $\alpha = k_4/k_1$. [O_2] and [L-Trp] are the initial concentrations of substrates.

We considered four models that differ in the magnitudes of k_2 and k_4. The values of k_1, k_{-1}, k_{-2}, k_3, and k_5 were set as described in the section on modeling the dependence of $^{Varied}k_{cat}/K_M$ on concentration of fixed substrate: $k_1 = 5.3 \times 10^5\ M^{-1}\ s^{-1}$, $k_{-1} = 6.8\ s^{-1}$, $k_{-2} = 501\ s^{-1}$, $k_3 = 4.37 \times 10^5\ M^{-1}\ s^{-1}$, and $k_5 = 8.3\ s^{-1}$. The results of modeling are presented in Fig. 5. Panels A and B show the outcomes for varied [L-Trp] and fixed [O_2] = 230 μM (which in our studies corresponds to air-saturation level of oxygen). Panel C visualizes the initial rates of oxygen consumption for varied O_2 at fixed 50.0 μM L-Trp.

In all panels in Fig. 5, the solid purple line corresponds to a model with $k_2 = 1.25 \times 10^6\ M^{-1}\ s^{-1}$ and $k_4 = 1.6 \times 10^5\ M^{-1}\ s^{-1}$ (Scheme 2). These values for the rate constants were introduced in the section on modeling the dependence of $^{Varied}k_{cat}/K_M$ on concentrations of fixed substrate. This model reproduces the initial rates for varied O_2 reasonably well (Fig. 5C). It also accurately replicates the values of k_{cat} and K_M for varied L-Trp: $^{Trp}k_{cat} = 7.8\ s^{-1}$ and $^{Trp}K_M = 19$ μM; however, the extent of *h*IDO1 inhibition by L-Trp, predicted by this model, is not as pronounced as the one observed experimentally. Here, $^{Trp}K_{SI} = 1260$ μM and $^{Trp}K'_{SI} = 1450$ μM (Fig. 5A and B, solid purple line). Also, the modeled ratio of $^{Trp}K'_{SI}$ to $^{Trp}K_{SI}$ differs significantly from the one found experimentally. Further analysis shows that simply decreasing the value of k_4 does not significantly improve the reproduction of the experimentally-observed inhibition (Fig. 5, light blue dash-dot line). In this model, k_4 was lowered to $7.1 \times 10^3\ M^{-1}\ s^{-1}$ – a value that replicates the experimental ratio of $^{Trp}K'_{SI}$ to $^{Trp}K_{SI}$, but not the magnitudes of these constants [71]. Simultaneous raising of k_2 and lowering of k_4 is in better agreement with the experiment. A model, where $k_2 = 3.6 \times 10^7\ M^{-1}\ s^{-1}$ and $k_4 = 7.1 \times 10^3\ M^{-1}\ s^{-1}$, gives $^{Trp}k_{cat} = 7.3\ s^{-1}$, $^{Trp}K_M = 17.4$ μM, $^{Trp}K_{SI} = 199$ μM, and $^{Trp}K'_{SI} = 1058$ μM, in good agreement with experimental data (Fig. 5, blue long-dashed line).

Global fit of the data from O_2 consumption-based assays

To further improve the agreement between the kinetic model in Scheme 2 and results of our assays, we performed a global fit of the data in Fig. 2 using OriginPro 2015 (Origin) from OriginLab. Data points in Fig. 1, shown by red circles, were also included in the fit. Initial rate of L-Trp dioxygenation was fitted as a function of two independent variables (initial concentrations of O_2 and L-Trp) and seven parameters (rate constants for the catalytic steps in Scheme 2). The details of the 3D surface fitting procedure are given in the Supporting Information [41].

An unconstrained fit, where all seven parameters are allowed to be optimized, results in very large standard errors for k_1, k_{-1}, k_2, and k_{-2}. Also, the magnitude of either k_2 or k_{-2} reaches a preset upper limit, where an increase in k_2 produces a compensating increase in k_{-2}, and vice versa. These observations suggest that parameters k_2 and k_{-2} are linked. These constants are the forward and reverse rate constants, respectively, for binding of L-Trp to free *h*IDO1. They are related by $^{Trp}K_d = k_{-2}/k_2$. Parameters k_1 and k_{-1} (the rate constants for binding and dissociation of O_2, respectively, to and from ferrous *h*IDO1) are related by a similar expression: $k_{-1}/k_1 = {}^{O_2}K_d$. Here, $^{O_2}K_d$ is an equilibrium constant for dissociation of O_2 from $^{Fe(III)}$*h*IDO1·O_2^-. The connection between the parameters k_2 and k_{-2} (as well as k_1 and k_{-1}) is further supported by the strong dependency values of 1, computed for k_1, k_{-1}, k_2, and k_{-2} in Origin.

In order to avoid ambiguity due to an inherent correlation between k_1 and k_{-1} and between k_2 and k_{-2}, we fixed the values of k_{-1} and k_{-2} during further fitting. The value of k_{-2} was set equal to $501\ s^{-1}$, which is a measured rate constant for dissociation of L-Trp from $^{Fe(II)}$*h*IDO1·CO·L-Trp [35]; k_{-1} was fixed at $4.84\ s^{-1}$ – a value that was obtained from unconstrained fits and that is in close agreement with the experimental dissociation rate constant: $k_{-1} = 6.8 \pm 1.8\ s^{-1}$ [26]. Global fitting with fixed k_{-1} and k_{-2} gives $k_1 = (1.83 \pm 0.64) \times 10^6\ M^{-1}\ s^{-1}$, $k_2 = (5.24 \pm 2.26) \times 10^7\ M^{-1}\ s^{-1}$, $k_3 = (5.05 \pm 0.20) \times 10^5\ M^{-1}\ s^{-1}$, $k_4 = (4.05 \pm 1.14) \times 10^3\ M^{-1}\ s^{-1}$, and $k_5 = 7.67 \pm 0.16\ s^{-1}$. These results are visualized in Fig. 6, where the calculated initial rates of O_2 consumption are plotted as solid lines together with the data from Fig. 2.

It is interesting to note here that global fitting gives the value of $^{Trp}K_d = 9.6 \pm 4.1$ μM and $^{O_2}K_d = 2.6 \pm 1.2$ μM, regardless of the constraints or preset limits for k_1, k_{-1}, k_2 and k_{-2}. The magnitude of $^{Trp}K_d$ for ferrous *h*IDO1 in the published literature ranges from 0.7 ± 0.2 μM to 530 ± 50 μM [23,72], highlighting the difficulty of analyzing small optical changes in the absorption of heme moiety upon binding of L-Trp to the free enzyme [23].

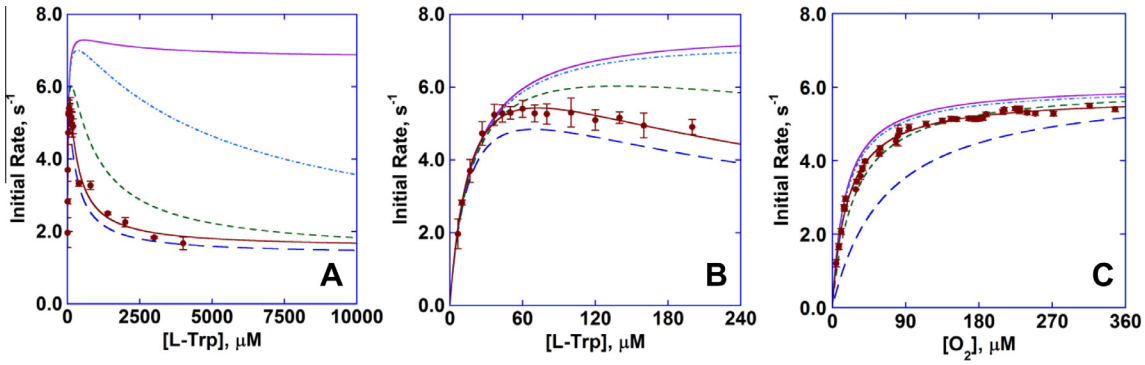

Fig. 5. Results of modeling the inhibition of *h*IDO1 by L-Trp. Red circles show the experimental data. (A) Varied L-Trp at fixed air-saturation level of $[O_2] = 230$ μM, (B) expansion of (A) from zero to 240 μM L-Trp, (C) varied O_2 at fixed [L-Trp] = 50.0 μM; the solid red line shows the best fit of the experimental data to Eq. (2) (A and B) and the Michaelis–Menten equation (C). The purple solid line corresponds to a model with $k_2 = 1.25\times10^6$ M^{-1} s^{-1} and $k_4 = 1.6\times10^5$ M^{-1} s^{-1}; light blue dash-dot line matches the model with $k_2 = 1.25\times10^6$ M^{-1} s^{-1} and $k_4 = 7.1\times10^3$ M^{-1} s^{-1}; green dashed line: $k_2 = 8.42\times10^6$ M^{-1} s^{-1} and $k_4 = 7.1\times10^3$ M^{-1} s^{-1}; blue long-dashed line: $k_2 = 3.6\times10^7$ M^{-1} s^{-1} and $k_4 = 7.1\times10^3$ M^{-1} s^{-1}. (For interpretation of the references to color in this figure legend, the reader is referred to the web version of this article.)

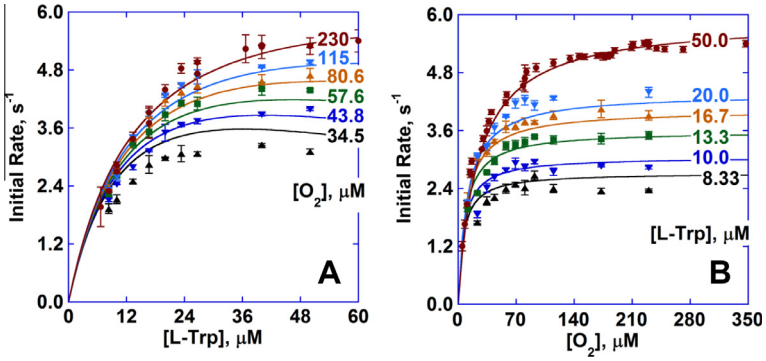

Fig. 6. Results of the global fit with fixed k_{-1} and k_{-2} (solid lines) overlaying the experimental data from Fig. 2 (colored symbols). The micromolar levels of the fixed substrate are displayed on the lines. (A) Varied L-Trp, fixed O_2; (●) correspond to 230 μM O_2, (▼) – 115 μM O_2, (▲) – 80.6 μM O_2, (■) – 56.7 μM O_2, (▼) – 43.8 μM O_2, and (▲) – 34.5 μM O_2. (B) Varied O_2, fixed L-Trp; (●) correspond to 50.0 μM L-Trp, (▼) – 20.0 μM L-Trp, (▲) – 16.7 μM L-Trp, (■) – 13.3 μM L-Trp, (▼) – 10.0 μM L-Trp, and (▲) – 8.33 μM L-Trp. (For interpretation of the references to color in this figure legend, the reader is referred to the web version of this article.)

As can be seen from the global fit, an accurate reproduction of experimental rates requires a kinetic model that features not only slow O_2 binding to $^{Fe(II)}$*h*IDO1·L-Trp, but also very fast binding of L-Trp to free $^{Fe(II)}$*h*IDO1.

Conclusion

In the current work, we analyzed enzyme kinetics of human indoleamine 2,3-dioxygenase as a function of O_2 and L-Trp, at physiologically-relevant concentrations of both substrates. Using a new assay methodology for the study of *h*IDO1 catalysis, we performed quantitative analysis of the effects of O_2 concentration on the initial rates. We analyzed the data within a mechanistic model, where the total velocity is a sum of two individual pathways with significantly disparate rates. The kinetic protocol described here also provides a powerful and convenient means to characterize the action of therapeutic *h*IDO1 inhibitors in the physiological ranges of both substrates free of cofactor interference. This approach has the potential to enhance drug design capabilities for a range of human pathologies driven by *h*IDO1.

Acknowledgments

We gratefully acknowledge Prof. A. Grant Mauk for the generous gift of *h*IDO1, cytochrome b_5, and cytochrome b_5 reductase expression vectors and helpful discussions; Profs. Bruce E. Bowler and Stephen R. Sprang for the use of stopped-flow systems and other major biochemical equipment in their laboratories, and helpful discussions. Research reported in this publication was supported by the National Institute of General Medical Sciences of the National Institutes of Health under Award Number P20GM103546 and the University of Montana. The content is solely the responsibility of the authors and does not necessarily represent the official views of the National Institutes of Health. Acquisition of the Bruker Microflex MALDI-ToF mass spectrometer was supported by the NSF CHE-1039814 award. Purchase of the AVIV Model 14 Spectrophotometer was supported by the NSF EPSCoR program under Grant # EPS-0701906 at the University of Montana.

Appendix A. Supplementary data

Supplementary data associated with this article can be found, in the online version, at http://dx.doi.org/10.1016/j.abb.2015.02.014.

References

[1] D. Voet, J.G. Voet, in: Biochemistry Volume One: Biomolecules, Mechanisms of Enzyme Action, and Metabolism, third ed., John Wiley & Sons, New York, NY, 2004, p. 1098.
[2] Ibid., p. 464.
[3] M. Berger, J.A. Gray, B.L. Roth, Annu. Rev. Med. 60 (2009) 355–366.
[4] A. Bertazzo, E. Ragazzi, M. Biasiolo, C.V.L. Costa, G. Allegri, Biochim. Biophys. Acta 1527 (2001) 167–175.
[5] H. Wolf, Scand. J. Clin. Lab. Invest. 33 (Suppl. 136) (1974) 11–182.

[6] M. Sono, M.P. Roach, E.D. Coulter, J.H. Dawson, Chem. Rev. 96 (1996) 2841–2887.
[7] T.L. Poulos, Chem. Rev. 114 (2014) 3919–3962.
[8] A. Mellor, Biochem. Biophys. Res. Commun. 338 (2005) 20–24.
[9] C.A. Opitz et al., Nature 478 (2011) 197–203.
[10] S. Vazquez, J.A. Aquilina, J.F. Jamie, M.M. Sheil, R.J.W. Truscott, J. Biol. Chem. 277 (2002) 4867–4873.
[11] B.D. Hood, B. Garner, R.J.W. Truscott, J. Biol. Chem. 274 (1999) 32547–32550.
[12] B. Wirleitner, G. Neurauter, K. Schroecksnadel, B. Frick, D. Fuchs, Curr. Med. Chem. 10 (2003) 1581–1591.
[13] J.M. Carlin, E.C. Borden, P.M. Sondel, G.I. Byrne, J. Immunol. 139 (1987) 2414–2418.
[14] A. Roth, P. König, G. van Zandbergen, M. Klinger, T. Hellwig-Bürgel, W. Däubener, M.K. Bohlmann, J. Rupp, Proc. Natl. Acad. Sci. U.S.A. 107 (2010) 19502–19507.
[15] A. Herbert, H. Ng, W. Jessup, M. Kockx, S. Cartland, S.R. Thomas, P.J. Hogg, O. Wargon, Br. J. Dermatol. 164 (2011) 308–315.
[16] S.K. Schmidt, S. Ebel, E. Keil, C. Woite, J.F. Ernst, A.E. Benzin, J. Rupp, W. Däubener, PLoS One 8 (5) (2013) e63301, http://dx.doi.org/10.1371/journal.pone.0063301.
[17] A. Carreau, B. El Hafny-Rahbi, A. Matejuk, C. Grillon, C. Kieda, J. Cell. Mol. Med. 15 (2011) 1239–1253.
[18] S. Yamamoto, O. Hayaishi, J. Biol. Chem. 242 (1967) 5260–5266.
[19] M. Sono, T. Taniguchi, Y. Watanabe, O. Hayaishi, J. Biol. Chem. 255 (1980) 1339–1345.
[20] M. Sono, J. Biol. Chem. 264 (1989) 1616–1622.
[21] M. Sono, Biochemistry 28 (1989) 5400–5407.
[22] C. Lu, S.-R. Yeh, J. Am. Chem. Soc. 131 (2009) 12866–12867.
[23] I. Efimov, J. Basran, X. Sun, N. Chauhan, S.K. Chapman, C.G. Mowat, E.L. Raven, J. Am. Chem. Soc. 134 (2012) 3034–3041.
[24] T. Taniguchi, M. Sono, F. Hirata, O. Hayaishi, M. Tamura, K. Hayashi, T. Iizuka, Y. Ishimura, J. Biol. Chem. 254 (1979) 3288–3294.
[25] M. Sono, Biochemistry 25 (1986) 6089–6097.
[26] N. Chauhan, J. Basran, I. Efimov, D.A. Svistunenko, H.E. Seward, P.C.E. Moody, E.L. Raven, Biochemistry 47 (2008) 4761–4769.
[27] A. Lewis-Ballester, D. Batabyal, T. Egawa, C. Lu, Y. Lin, M.A. Marti, L. Capece, D.A. Estrin, S.-R. Yeh, Proc. Natl. Acad. Sci. U.S.A. 106 (2009) 17371–17376.
[28] R.M. Davydov, N. Chauhan, S.J. Thackray, J.L.R. Anderson, N.D. Papadopoulou, C.G. Mowat, S.K. Chapman, E.L. Raven, B.M. Hoffman, J. Am. Chem. Soc. 132 (2010) 5494–5500.
[29] A.J. Muller, J.B. DuHadaway, P.S. Donover, E. Sutanto-Ward, G.C. Prendergast, Nat. Med. 11 (2005) 312–319.
[30] S.V. Novitskiy, H.L. Moses, Cancer Discov. 2 (2012) 673–675.
[31] R.B. Holmgaard, D. Zamarin, D.H. Munn, J.D. Wolchok, J.P. Allison, J. Exp. Med. 210 (2013) 1389–1402.
[32] Here, we designate the ferrous *h*IDO1 adduct with O_2 as $^{Fe(III)}$*h*IDO1·O_2^- to indicate that it exhibits $Fe^{(III)}$–O_2^- rather than $Fe^{(II)}$–O_2 character, based on recent resonance Raman studies [27].
[33] S. Yanagisawa, M. Horitani, H. Sugimoto, Y. Shiro, N. Okada, T. Ogura, Faraday Discuss. 148 (2011) 239–247.
[34] S. Yanagisawa, M. Hara, H. Sugimoto, Y. Shiro, T. Ogura, Chem. Phys. 419 (2013) 178–183.
[35] B. Weber, E. Nickel, M. Horn, K. Nienhaus, G.U. Nienhaus, J. Phys. Chem. Lett. 5 (2014) 756–761.
[36] B. Widner, E.R. Werner, H. Schennach, H. Wachter, D. Fuchs, Clin. Chem. 43 (1997) 2424–2426.
[37] B.K. Madras, E.L. Cohen, R. Messing, H.N. Munro, R.J. Wurtman, Metabolism 23 (1974) 1107–1116.
[38] F.I. Rosell, H.H. Kuo, A.G. Mauk, J. Biol. Chem. 286 (2011) 29273–29283.
[39] E. Lloyd, J.C. Ferrer, W.D. Funk, M.R. Mauk, A.G. Mauk, Biochemistry 33 (1994) 11432–11437.
[40] L.A. Trepanier, S.U. Bajad, J.R. Kurian, Evaluation of the cytochrome b5/cytochrome b5 reductase pathway, in: L.G. Costa, J.C. Davila, D.A. Lawrence, D.J. Reed (Eds.), Current Protocols in Toxicology, Supplement 24, John Wiley & Sons, 2005, pp. 4.16.1–4.16.17 (doi: 10.1002/0471140856.tx0416s24).
[41] See Supporting Information.
[42] YSI, Inc., The Dissolved Oxygen Handbook: a Practical Guide to Dissolved Oxygen Measurements, 2009, p. 46.
[43] A. Grant Mauk, personal communication.
[44] N.D. Papadopouolu, M. Mewies, K.J. McLean, H.E. Seward, D.A. Svistunenko, A.W. Munro, E.L. Raven, Biochemistry 44 (2005) 14318–14328.
[45] R.M.C. Dawson, D.C. Elliott, W.H. Elliott, K.M. Jones, Data for Biochemical Research, third ed., Oxford University Press, USA, 1989. p. 122.
[46] Y. Ishimura, M. Nozaki, O. Hayaishi, T. Nakamura, M. Tamura, I. Yamazaki, J. Biol. Chem. 245 (1970) 3593–3602.
[47] M. Sono, S.G. Cady, Biochemistry 28 (1989) 5392–5399.
[48] E. Vottero, D.A. Mitchell, M.J. Page, R.T. MacGillivray, I.J. Sadowski, M. Roberge, A.G. Mauk, FEBS Lett. 580 (2006) 2265–2268.
[49] G.J. Maghzal, S.R. Thomas, N.H. Hunt, R. Stocker, J. Biol. Chem. 283 (2008) 12014–12025.
[50] S. Yanagisawa, K. Yotsuya, Y. Hashiwaki, M. Horitani, H. Sugimoto, Y. Shiro, E.H. Appelman, T. Ogura, Chem. Lett. 39 (2010) 36–37.
[51] J.T. Pearson, S. Siu, D.P. Meininger, L.C. Wienkers, D.A. Rock, Biochemistry 49 (2010) 2647–2656.
[52] W.W. Cleland, Steady state kinetics, in: P.D. Boyer (Ed.), The Enzymes, Volume II, Kinetics and Mechanism, Academic Press, New York, NY, 1970, p. 1.
[53] The derivation of Eq. (2) is shown in the Supporting Information, see Eq. (S13) [41].
[54] H.J. Fromm, Initial Rate Enzyme Kinetics, Springer-Verlag, Berlin, Germany, 1975. p. 49.
[55] C. Lu, S.-R. Yeh, Biochemistry 49 (2010) 5028–5034.
[56] The derivation of Eq. (6) is presented in the Supporting Information, see Eq. (S20) [41].
[57] For the derivation of Eq. (4) see Eq. (S18) in the Supporting Information [41].
[58] The derivation of Eqs. (4) through (9) is shown in the Supporting Information, see Eqs. (S18), (S19), (S20), (S29), (S30), and (S33), respectively [41].
[59] S.G. Cady, M. Sono, Arch. Biochem. Biophys. 291 (1991) 326–333.
[60] N. Chauhan, S.J. Thackray, S.A. Rafice, G. Eaton, M. Lee, I. Efimov, J. Basran, P.R. Jenkins, C.G. Mowat, S.K. Chapman, E.L. Raven, J. Am. Chem. Soc. 131 (2009) 4186–4187.
[61] H.J. Fromm, Initial Rate Enzyme Kinetics, Springer-Verlag, Berlin, Germany, 1975. p. 94.
[62] P.F. Cook, W.W. Cleland, Enzyme Kinetics and Mechanism, Garland Science, New York, NY, 2007. p. 157.
[63] A. Cornish-Bowden, Biochem. J. 137 (1974) 143–144.
[64] P.F. Cook, W.W. Cleland, Enzyme Kinetics and Mechanism, Garland Science, New York, NY, 2007. p. 76.
[65] I.H. Segel, Enzyme Kinetics: Behavior and Analysis of Rapid Equilibrium and Steady-State Enzyme Systems, John Wiley & Sons, New York, NY, 1975. p. 646.
[66] The magnitude of k_{-1} (Scheme 2) is expected to be pH-independent between 6.5 and 8.0, because in $^{Fe(III)}$*h*IDO1·O_2^- the frequency of $\nu_{Fe\text{-}O2}$ mode is pH-independent in the same range [33].
[67] W. Ferdinand, Biochem. J. 98 (1966) 278–283.
[68] I.H. Segel, Enzyme Kinetics: Behavior and Analysis of Rapid Equilibrium and Steady-State Enzyme Systems, John Wiley & Sons, New York, NY, 1975. p. 657.
[69] For the derivation of Eq. (11) see Eq. (S22) in the Supporting Information [41].
[70] For the origin of Eq. (12) see the derivation of Eq. (S9) in the Supporting Information [41].
[71] Obtained by dividing Eq. (S22) by Eq. (S21) and solving the resulting ratio for k_4 [41].
[72] H. Sugimoto, S.-I. Oda, T. Otsuki, T. Hino, T. Yoshida, Y. Shiro, Proc. Natl. Acad. Sci. U.S.A. 103 (2006) 2611–2616.